

Synthesis of Gadolinium-enhanced Liver Tumors on Nonenhanced Liver MR Images Using Pixel-level Graph Reinforcement Learning

Chenchu Xu^{a,b,*}, Dong Zhang^{b,*}, Jaron Chong^b, Bo Chen^{c,**}, Shuo Li^{b,**}

^a*School of Computer Science and Technology, Anhui University, Hefei, China*

^b*Department of Medical Imaging, Western University, London ON, Canada*

^c*School of Health Science, Western University, London ON, Canada*

Abstract

If successful, synthesis of gadolinium (Gd)-enhanced liver tumors on nonenhanced liver MR images will be critical for liver tumor diagnosis and treatment. This synthesis will offer a safe, efficient, and low-cost clinical alternative to eliminate the use of contrast agents in the current clinical workflow and significantly benefit global healthcare systems. In this study, we propose a novel pixel-level graph reinforcement learning method (Pix-GRL). This method directly takes regular nonenhanced liver images as input and outputs AI-enhanced liver tumor images, thereby making them comparable to traditional Gd-enhanced liver tumor images. In Pix-GRL, each pixel has a pixel-level agent, and the agent explores the pixel's features and outputs a pixel-level action to iteratively change the pixel value, ultimately generating AI-enhanced liver tumor images. Most importantly, Pix-GRL creatively embeds a graph convolution to represent all the pixel-level agents. A graph convolution is deployed to the agent for feature exploration to improve the effectiveness through the aggregation of long-range contextual features, as well as outputting the action to enhance the efficiency through shared parameter training between agents. Moreover, in our Pix-GRL method, a novel reward is used to measure pixel-level action to significantly improve the performance by considering the improvement in each action in each pixel with its own future state, as well as those of neighboring pixels. Pix-GRL sig-

*These authors contributed equally to this work.

**Corresponding author

Email address: slishuo@gmail.com (Shuo Li)

nificantly upgrades the existing medical DRL methods from a single agent to multiple pixel-level agents, becoming the first DRL method for medical image synthesis. Comprehensive experiments on three types of liver tumor datasets (benign, cancerous, and healthy controls) with 325 patients (24,375 images) show that our novel Pix-GRL method outperforms existing medical image synthesis learning methods. It achieved an SSIM of 0.85 ± 0.06 and a Pearson correlation coefficient of 0.92 in terms of the tumor size. These results prove that the potential exists to develop a successful clinical alternative to Gd-enhanced liver MR imaging.

Keywords: Gadolinium-enhanced liver tumor imaging, Deep reinforcement learning, Graph convolution, Pixel-level agents, Complementary reward

1. Introduction

If successful, synthesis of gadolinium (Gd)-enhanced liver tumors on non-enhanced liver MR images will be critical for liver tumor diagnosis and treatment (Huppertz et al., 2004; Kuo et al., 2007). This synthesis aims to generate an image that can help clinicians accurately observe and diagnose a tumor, similar to Gd-enhanced live MRI, by inputting only a regular non-enhanced liver MRI. As shown in Fig. 1, this synthesis will offer a safe, efficient, and low-cost clinical alternative for eliminating the use of contrast agents (CAs) in the current clinical workflow (Abubakar et al., 2015; El-Serag et al., 2008). It will eliminate CA-associated issues. 1) One such issue is the potential toxicity. CA, with its metal compounds, causes allergy-like reactions, gadolinium retention, and even fatal nephrogenic systemic fibrosis in patients with compromised kidney function. More than 17% of patients with liver disease have kidney disease (Lauenstein et al., 2015). 2) Another

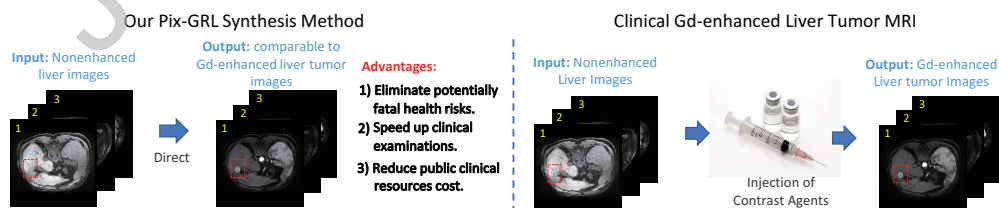


Figure 1: A potential clinical alternative is proposed to eliminate the use of CAs in Gd-enhanced liver tumor MR imaging. This method prevents Gd-associated health risks and streamlines clinical workflows.

15 CA-associated issue is the high time consumption. CA injection requires
 16 additional patient time and causes discomfort. Improper injection results
 17 in wasted MR scanner time and rescheduling another scan (Reimer et al.,
 18 2004). 3) Finally, CAs are expensive. In the United States, each dose of
 19 CA costs more than \$70. This does not include the indirect costs associated
 20 with operational inefficiencies. In developing countries, both MR machines
 21 and CA are imported, and the cost per dose will be even higher (von Herbay
 22 et al., 2002).

23 Rough enhanced liver tumor images (Fig. 2) have recently been syn-
 24 thesized on nonenhanced liver images (Zhao et al., 2020). But these rough
 25 enhanced images are just the intermedia auxiliary for tumor segmentation,
 26 which focuses only on the tumor structural information. Thus, synthesis of
 27 the internal diagnostic details of the tumors still an open challenge, such
 28 as infiltrative growth but also the internal diagnostic details, such as the
 29 capsule surrounding the tumor. According to the Liver Imaging Reporting
 30 and Data System (LI-RADS, the tumor staging standard) (Kinoshita et al.,
 31 2015), the tumor contextual details are basic metrics (Duseja, 2014), and
 32 crucial content to tumor diagnosis (benign or cancerous). Thus, clinicians
 33 urgently desire the development of a more advanced Gd-free technology to

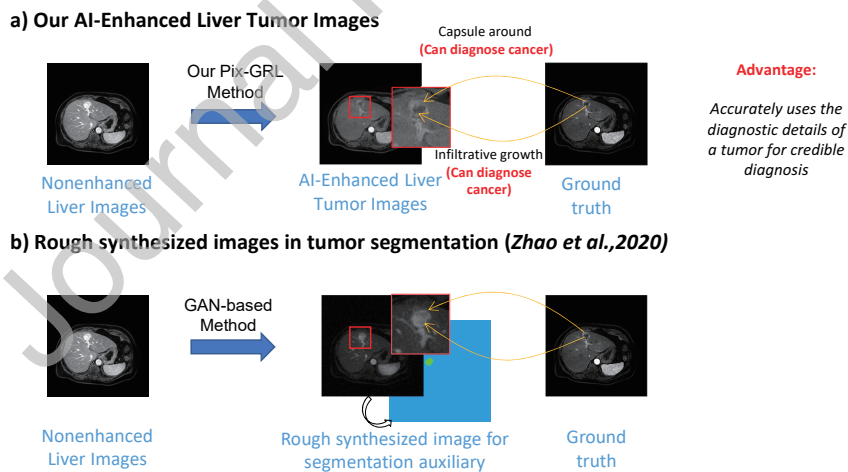


Figure 2: Pix-GRL as a Gd-free synthesis technology for generating Gd-enhanced liver tumors on nonenhanced liver MR images. It provides accurate tumor diagnostic detail comparable to clinical Gd-enhanced tumor imaging for credible diagnosis, rather than only a rough synthesized image as auxiliary information for segmentation.

34 synthesize enhanced tumor images with accurate diagnostic details.

35 Synthesis of a Gd-enhanced liver tumor image with accurate diagnostic
 36 detail has multiplex challenges: 1) some tissues are invisible before CA injec-
 37 tion (Fig. 3). CA greatly changes the appearance of almost all tissues and
 38 even presents some tissues that cannot be invisible before CA injection (i.e.,
 39 input) (Xiao et al., 2019). This invisibility causes errors in the initial feature
 40 space of the tissues in the input and may lead to misunderstandings during
 41 synthesis. 2) Diagnostic details are too small in the image (Fig. 3). Diag-
 42 nostic details make up an average of only 2% of pixels in an image. These
 43 very small details may be interfered with by the remaining tissues during
 44 synthesis (Zhao et al., 2020).

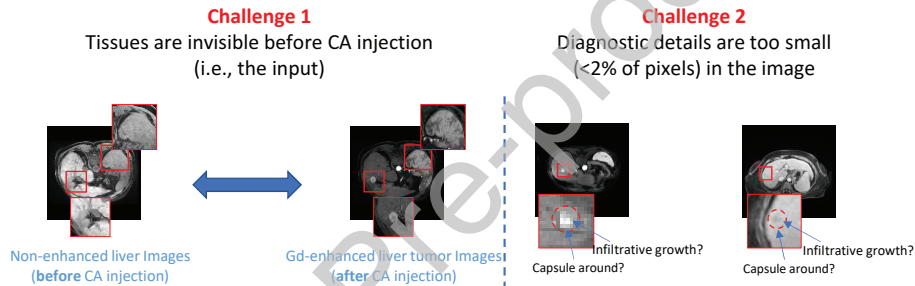


Figure 3: Synthesis of a Gd-enhanced liver tumor image with accurate diagnostic detail has multiple challenges: 1) some tissues are invisible before CA injection (red line), and 2) diagnostic details are too small (they make up less than 2% of the pixels in the image, red dashed line)

45 Even recent advanced image-to-image medical image synthesis methods
 46 often fail for very small objects with very small sizes and invisible appearances
 47 (Arora et al., 2017). The reason is because most of these methods rely on
 48 generative adversarial networks (GANs), while 1) GANs are not naturally
 49 good at synthesizing small details (Arora et al., 2017). A GAN is an overall
 50 image distribution distance optimization technology (Nie et al., 2017) that
 51 is good at global and whole quality synthesis, but it is often limited by the
 52 synthesis of small objects caused by the local details of these small objects'
 53 weak contributions to global optimization (Arora et al., 2017). 2) Recent
 54 improvements to GANs for very small objects cannot be applied to invisible
 55 objects in the input. Recent GAN methods use the appearance of objects
 56 (such as segmentation and colors) to build a constraint model (Isola et al.,
 57 2017) or loss terms (Choi et al., 2018) to improve the understanding of small

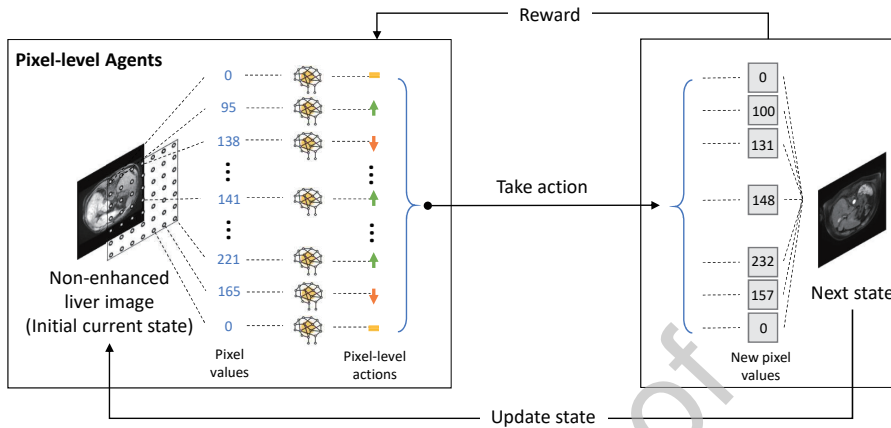


Figure 4: Our Pix-GRL method explores the features of each pixel during the iterative process to output the action for each pixel, thereby updating the state by simultaneously changing the pixel value of each pixel. A nonenhanced liver image is the initial current state. Our Pix-GRL can find a set of optimal actions to iteratively update the state to generate high-quality AI-enhanced liver images under nonenhanced liver image guidance.

58 objects and facilitate synthesis. However, the issue of object invisibility in the
 59 input blocks these GANs from obtaining the accurate appearance of objects
 60 and leads to ineffectiveness of the constraint model or loss terms.

61 Deep reinforcement learning (DRL) has shown impressive performance on
 62 objects with very small sizes and invisible appearances (Ghesu et al., 2016;
 63 Alansary et al., 2019). DRL has the ability to iteratively explore tasks with
 64 an artificial agent in wider dynamic feature spaces with a Markov decision-
 65 making process (Mnih et al., 2015) instead of traditional simple nonlinear
 66 mapping in deep learning technology, including GANs. These artificial agents
 67 do not need labeled input/output pairs and 1) focus on the task’s object opti-
 68 mization rather than global function approximation to handle very small
 69 objects (Ghesu et al., 2016). 2) They can also self-explore knowledge of ob-
 70 jects without insensitivity to the input feature space of its input appearance
 71 to handle the invisible appearance in the input (Alansary et al., 2019). Thus,
 72 in our work, DRL has great potential to synthesize AI-enhanced liver tumor
 73 images with accurate diagnostic detail on nonenhanced liver images under
 74 the guidance of Gd-enhanced liver MR images.

75 Unfortunately, there are still no DRL methods reported for medical image
 76 synthesis. Existing medical DRL approaches for a single agent (Ghesu et al.,
 77 2017; Maicas et al., 2017; Ghesu et al., 2016) focus on a region of interest, and

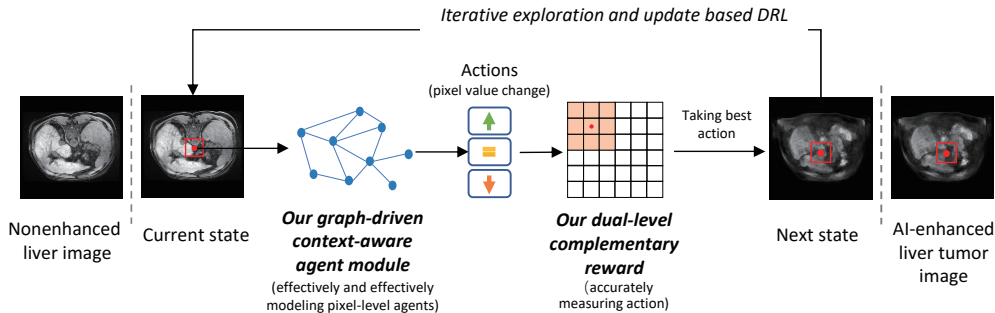


Figure 5: Our Pix-GRL proposes two novelties to improve its performance. They are: 1) a novel graph-driven context-aware agent module to achieve the high-effective state feature exploring and high-efficient pixel-level action outputting; 2) a novel dual-level complementary reward to optimize each agent to improve the accuracy of the optimal action measurement.

78 they are incapable of addressing pixel-level medical image synthesis. Thus, a
 79 DRL method with multiple (pixel-level) agents is necessary, where every single
 80 agent focuses on every pixel so that all the agents can output the ultimate
 81 accurate synthetic image. However, employing pixel-level agents requires 1)
 82 exploring ambiguous features between and within pixels. To employ pixel-
 83 level agents, each pixel requires exploration in isolation. However, local pixel
 84 evidence is ambiguous in the liver when each pixel is isolated, and local pixel
 85 features interfere with one another (Zhang et al., 2019b); 2) high algorithm
 86 complexity and computational cost should be avoided. To deploy pixel-level
 87 agents, all pixel-level agents require training simultaneously. However, the
 88 number of pixels in an MR image is extremely large (a 256×256 image
 89 requires 65,536 agents). The training of all these pixel-level agents has high
 90 algorithm complexity and computational cost.

91 In this paper, we propose a novel pixel-level graph reinforcement learn-
 92 ing network (Pix-GRL) that directly inputs regular nonenhanced liver tumor
 93 images and outputs AI-enhanced liver tumor images, which are comparable
 94 to traditional Gd-enhanced liver tumor images. Our Pix-GRL method, for
 95 the first time, creatively integrates a graph convolution into DRL for medical
 96 image synthesis. Herein, each pixel has a pixel-level agent, and each agent
 97 is based on the graph convolution to explore the pixel features and predict
 98 a pixel-level action. After all the pixel-level agents find optimal pixel-level
 99 actions that have the greatest long-term rewards, Pix-GRL takes these ac-
 100 tions to iteratively change the value of each pixel to generate high-quality

101 AI-enhanced liver tumor images.

102 Specifically, Pix-GRL uses a novel graph-driven context-aware agent mod-
103 ule to integrate graph convolution into DRL to represent all pixel-level agents.
104 This module allows each pixel-level agent to benefit from the abilities of
105 the node feature aggregation and the shared node weight parameters of the
106 graph convolution during state exploration and action training, respectively
107 . Thus, each pixel-level agent has the ability to effectively explore its own
108 pixel’s intrinsic long-range contextual features in a given state, avoiding the
109 interference caused by ambiguous local features between and within pix-
110 els. Additionally, All pixel-level agents can be efficiently trained and out-
111 put pixel-level actions for each pixel simultaneously using a shared training
112 weight. This approach avoids the high algorithm complexity and computa-
113 tional cost caused by a large number of agents. Moreover, Pix-GRL uses a
114 novel dual-level complementary reward to improve the accuracy of finding
115 optimal pixel-level actions, boosting the agents’ optimization. The reward
116 combines a pixel-level reward function and a region-level reward function in
117 action measuring to consider not only each pixel with its own future state but
118 also those of neighboring pixels. It ensures that each agent pays attention to
119 both the content details of each pixel and the local texture details of pixels
120 during optimization while avoiding agents from falling into local optima.

121 1.1. Contributions

122 In summary, the main contributions of this work are as follows:

- 123 • For the first time, Gd-free imaging technology can be used to generate
124 output comparable to liver tumor contrast-enhanced imaging. This
125 technology offers a safe, efficient, and low-cost clinical alternative to
126 eliminate Gd-associated health risks, streamline clinical workflows and
127 conserve clinical resources.
- 128 • For the first time, a pixel-level action-based DRL method is proposed
129 for medical image analysis. It enables medical image synthesis to re-
130 quire pixel-level actions, significantly improving existing medical DRL
131 methods that can execute only global actions for the entire image.
- 132 • A novel graph-driven context-aware agent module is proposed for highly
133 effective feature exploration and highly efficient action obtainment. It
134 not only aggregates long-range contextual features to avoid interference
135 between ambiguous local features but also shares the agent’s parameter

136 weights as a convolutional operation to reduce the algorithm complex-
 137 ity.

- 138 • A novel dual-level complementary reward is proposed for agent opti-
 139 mization to keep the agents from falling into local optima during train-
 140 ing. It considers not only the future state of its own pixel but also
 141 those of neighboring pixels in reward computation.

142 2. Related work

143 2.1. Existing of liver tumor image synthesis and analysis methods

144 Our approach is a pioneering work on the synthesis of Gd-enhanced liver
 145 tumor images without CA, but various liver tumor analysis methods have
 146 been published currently. Most of these published methods, such as tumor
 147 segmentation (Xiao et al., 2019; Budak et al., 2020), tumor quantification
 148 (Cano-Espinosa et al., 2020), and tumor classification (Zhen et al., 2020), are
 149 performed on Gd-enhanced images. These methods significantly promote the
 150 progress of liver tumor analysis, especially liver cancer diagnosis. However,
 151 they still struggle with the potential toxicity, high time consumption, and
 152 expense of using CA in Gd-enhanced imaging (Xu et al., 2020). Recently,
 153 harnessing the power of deep learning development, two proposed methods
 154 have successfully segmented liver tumors without CA. The first method en-
 155 tails learning the correlation of the radiomics features between the nonen-
 156 hanced liver image and the Gd-enhanced liver image to enable CA-free tumor
 157 segmentation to a binary image. However, the resulting binary segmentation
 158 image cannot provide sufficient diagnostic information for a credible tumor
 159 diagnosis. The second method is described in the work of (Zhao et al., 2020),
 160 which introduces synthesized rough enhanced liver tumor images to improve
 161 tumor segmentation performance. However, as mentioned above, these rough
 162 enhanced images lack important details for tumor diagnosis; thus, the clinical
 163 significance of these images is limited.

164 2.2. Graph convolutional network in pixel relationship modeling

165 A graph convolutional network (Wang et al., 2018) is able to model the
 166 relationship between pixels more efficiently to capture contextual informa-
 167 tion to assess small objects (Zhang et al., 2019b) than recent representation
 168 learning frameworks. These frameworks include 1) fully convolutional net-
 169 works (FCNs) (Long et al., 2015), 2) dilated convolutions (Yu and Koltun,

170 2015) and 3) self-attention mechanisms (Zhang et al., 2019a). Currently,
171 most methods are based on deep learning using FCNs to learn the relation-
172 ship between pixels. However, the receptive field of an FCN grows slowly
173 (only linearly) with increasing network depth, and its limited receptive field
174 is not able to capture longer-range relationships between pixels in an image.
175 Dilated convolutions have been proposed to enlarge the receptive field during
176 learning (Ge et al., 2019b,a). However, the resulting feature representation is
177 dominated by large objects in the image, and consequently, the performance
178 on small objects is poor (Hamaguchi et al., 2018; Zhang et al., 2020b). Self-
179 attention mechanisms have been used to model each spatial position with
180 its long-distance neighbors. However, the large affinity matrix during mod-
181 eling resulted in high memory requirements and was not suitable for DRL,
182 which also consumes a considerable amount of memory (Cordts et al., 2016;
183 Zhang et al., 2020c). In contrast, a graph convolutional network leverages
184 the layerwise propagation rule, which can globally propagate information of
185 each pixel to the whole image conditional on the input in low-cost memory
186 computations.

187 *2.3. Deep reinforcement learning in medical image analysis*

188 Recently, deep reinforcement learning (DRL) has shown impressive per-
189 formance in a variety of medical image processing tasks, including target
190 object tracking (Luo et al., 2019), detection tasks (Maicas et al., 2017) and
191 segmentation (Tian et al., 2020; Zhang et al., 2020a). DRL, as a well-known
192 unconstrained optimization technology, has the advantage of optimizing the
193 task in continuously changing feature spaces by making a sequence of de-
194 cisions (Ghesu et al., 2016). Thus, it can avoid suboptimal optimization
195 and overfitting caused by current fully supervised deep learning solutions
196 with only a single decision feature space during global optimization, thereby
197 achieving better performance (Ghesu et al., 2016). However, no DRL has
198 been reported for medical image synthesis so far. Existing medical DRL
199 methods focus only on object detection and segmentation with very few
200 isolated agents and have an inability to synthesize images, which requires
201 training an extremely large number of independent agents to pixel-level ma-
202 nipulations. Thus, these medical DRL methods cannot be applied for medical
203 image synthesis.

204 2.4. Decision process of deep reinforcement learning

205 Deep reinforcement learning combines artificial neural networks with a
 206 reinforcement learning architecture that trains agents to attain defined goals.
 207 DRL regards agent training as a Markov decision process problem denoted
 208 by $\{s, a, r, \pi\}$. s is the **state** space, which is the input of the agents. In our
 209 work, s is always a 2D image, where s_i denotes the i -th pixel in the input
 210 state that has N pixels ($i = 1, \dots, N$). a is the **action**, and agents take the
 211 actions by learning the states. It changes the state s_i^t in time step t to the
 212 next state s_i^{t+1} . In our work, $a^t \in (a_i^t, \dots, a_N^t)$ denotes the change in each
 213 pixel value (increasing, decreasing, or does not change). r is the **reward**,
 214 which is the feedback given by measuring the success or failure of an agent’s
 215 actions in a given state. In our work, $r \in (r_i^t, \dots, r_N^t)$ denotes the action’s
 216 contribution to reducing the distance between the pixel value in the given
 217 state and the value in the Gd-enhanced liver tumor image. π is the **policy**
 218 that the agent employs to determine the next action based on the current
 219 state. $\pi(a^t|s^t)$ maps states to actions. The objective of Pix-GRL is to learn
 220 the optimal policies $\pi = (\pi_1, \dots, \pi_N)$ for each pixel.

221 The fundamental concept of our Pix-GRL is inspired by the actor-critic
 222 architecture. This architecture is one of the most effective and reliable meth-
 223 ods in DRL. In this architecture, two models are constructed, namely, the
 224 actor and the critic. The actor takes the state as input and outputs the
 225 best action. The critic evaluates the action by computing the value function.
 226 The advantage of this architecture is that it combines the superior features
 227 of existing value-based and policy-based DRL methods. This architecture
 228 trains two models by conducting a game to enable interaction of the actions
 229 and the values of those actions. Thus, it can control the agent to learn an
 230 explicitly stochastic policy and successfully resolves the instability and high
 231 computational cost of action selection.

232 3. Methodology

233 Pix-GRL (Fig. 6) consists of a graph-driven context-aware agent module
 234 (Sect. 3.1) and a dual-level complementary reward-based advantage func-
 235 tion (Sect. 3.2). The graph-driven context-aware agent module effectively
 236 explores the features of each pixel to efficiently obtain the pixel-level ac-
 237 tions. It is performed by two networks: a state-behavior network and a
 238 state-evaluator network. The dual-level complementary reward-based advan-
 239 tage function measures all the pixel-level actions to reciprocally train these

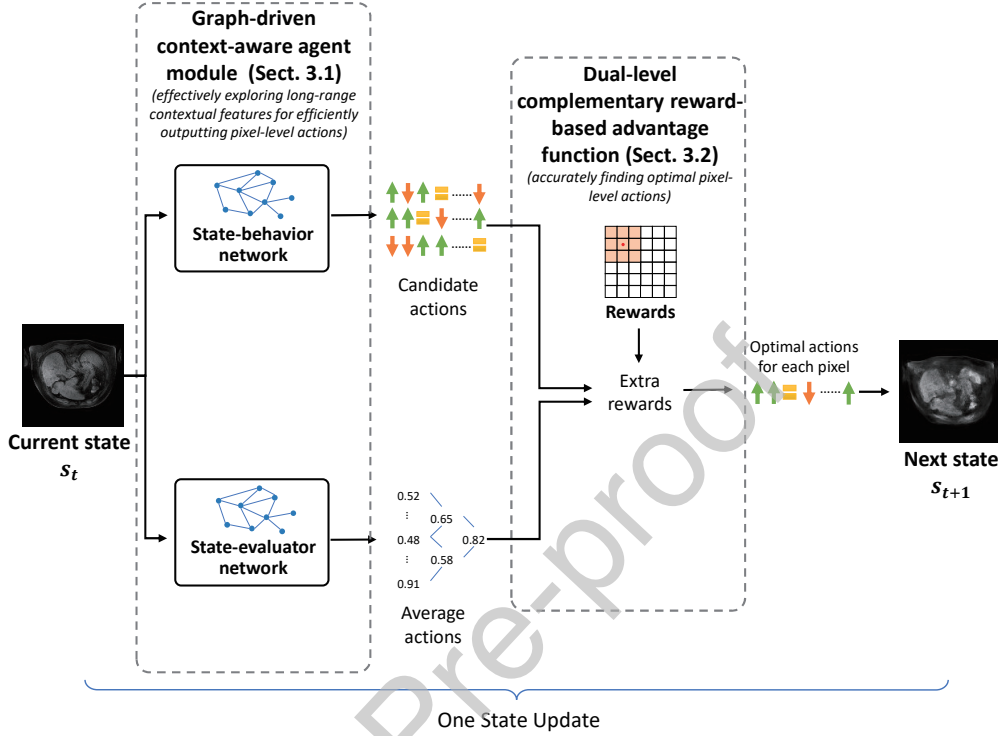


Figure 6: In each state update, Pix-GRL consists of a graph-driven context-aware agent module and a dual-level complementary reward-based advantage function. The novel graph-driven context-aware agent module is used to efficiently and effectively explore the given state to obtain the independent output to each pixel of that state. The dual-level complementary reward-based advantage function is used to accurately measure all actions to find the optimal action to update the state.

240 two networks and accurately find the optimal action to update the state. It
 241 is divided into two steps: a dual-level complementary reward computation
 242 and an advantage function computation.

243 Let a nonenhanced liver image be the initial current state. In the *train-*
 244 *ing phase*, the state-behavior network estimates pixel-level candidate actions
 245 of the current state by observing the current state. The state-evaluator net-
 246 work predicts a pixel-level average action as an empirical baseline that would
 247 have been taken at the current state. With the dual-level complementary re-
 248 ward measuring the improvement in two kinds of image synthesis actions,
 249 the advantage function computes the extra rewards by comparing the real
 250 rewards of the candidate actions with the expected rewards of the average

251 action. It finds whether the candidate actions have resulted in better or
 252 worse results than the baseline action and takes the optimal action that has
 253 the most extra rewards to update the current state to the next state. Mean-
 254 while, the advantage function feeds back to optimize both networks, namely,
 255 the advantage function enables the state-behavior network to estimate better
 256 candidate actions and enables the state-evaluator network to predict more
 257 accurate average actions, thereby computing an accurate advantage function
 258 to find an optimal action at the next state. The above process is repeated
 259 iteratively until a series of optimal actions are found to update the current
 260 state to Gd-enhanced liver tumor images. In the *testing phase*, the trained
 261 state-behavior network directly outputs a series of pixel-level actions to up-
 262 date the current state to AI-enhanced liver tumor images according to the
 263 optimal actions of that state found in the training phase.

264 3.1. Graph-driven context-aware agent module for estimating pixel-level ac- 265 tions

266 To enable the pixel-level agent to effectively explore the synthesis of
 267 required features and efficient output actions for each pixel of the current
 268 state, Pix-GRL embeds FC graph convolutions to build a novel graph-driven
 269 context-aware agent module (Fig. 8). This module is a pixel-level encoder-
 270 decoder network, which takes each pixel as a node and encodes the features
 271 to decode an action for each pixel, as shown in Fig. 7. Benefiting from all the
 272 states and outputs (actions, rewards, and state values), this module lever-
 273 ages the manner of convolution operation in a matrix to endow pixel-level
 274 agents to aggregate long-range contextual features of each pixel during state
 275 exploration. It also shares the weight parameters to represent all the actions
 276 during training a large number of agents (65,536 agents, where the number
 277 of agents equals the number of pixels).

278 The graph-driven context-aware agent module is performed by two net-
 279 works, namely, the state-behavior network and the state-evaluator network.
 280 These two networks take the current state as input, estimate pixel-level can-
 281 didate actions, and predict the pixel-level average actions for each pixel of
 282 that state. They have very similar network structures; that is, the same
 283 FC graph convolution-based layers are used for feature exploration, and the
 284 following softmax or regression layers are used for different outputs. Neither
 285 network includes any dimension reduction operation (pooling or stride) to
 286 ensure not only the feature propagation independence of each pixel location

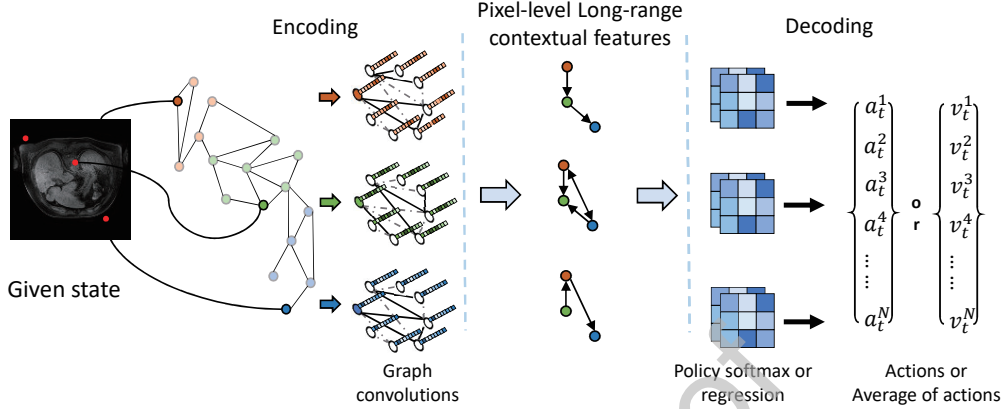


Figure 7: Our graph-driven context-aware agent module creatively incorporates graph convolution into DRL to enable pixel-level agents to effectively explore each pixel’s current state and efficiently obtain pixel-level actions. The framework endows all the agents (65,536 agents, which equals the number of pixels) to explore long-range contextual features of each pixel by leveraging node feature aggregation and shares the weight parameters of all the actions by representing the same weight to all the agents as a convolution operation.

287 during the current state exploration but also the propagation independence
 288 of each agent feature during global state iterative updating.

289 3.1.1. FC graph convolution-based effective state exploration

290 Our graph-driven context-aware agent module combines two FC convolu-
 291 tions and three FC graph convolutions to effectively explore the long-range
 292 contextual features of each pixel in the current state. An FC convolution
 293 is a typical convolutional operation, but it does not use any operation to
 294 reduce the number of feature dimensions. It is based on the receptive field
 295 to learn the features of the local region of each pixel in an image. The graph
 296 convolution layer is a highly efficient, effective, and differentiable layer. It
 297 generalizes the pixel relationship with a neighborhood definition conditional
 298 on the input and allows long-range information exchange in a single layer to
 299 improve convolution effectiveness. By combining a graph convolution and an
 300 FC convolution, our graph-driven context-aware agent module can use the
 301 spectral rule to aggregate the feature space of interdependencies along the
 302 channel dimensions of the convolution’s feature map. It enables each pixel-
 303 level agent to explore coherent relationships by considering all the pixels in

304 the image. This spectral rule can be expressed as:

$$\begin{aligned} \text{aggregate}(\mathcal{A}, \mathcal{X})_i &= \mathcal{D}^{-0.5} \mathcal{A}_i \mathcal{D}^{-0.5} \mathcal{X} \\ &= \sum_{j=1}^{\mathcal{N}} \frac{1}{\mathcal{D}_{i,i}^{0.5}} \mathcal{A}_{i,j} \frac{1}{\mathcal{D}_{j,j}^{0.5}} \mathcal{X}_j, \end{aligned} \quad (1)$$

305 where \mathcal{X}_i is the input features of the i -th node, and \mathcal{D} is the degree matrix
 306 used to transform the adjacency matrix \mathcal{A} to the power of -0.5. . This rule
 307 ensures that not only the degree of the i -th node but also the degree of the
 308 j -th node is considered when aggregating features of the i -th node.

309 Specifically, it takes the current state as input and includes two steps.
 310 Let the inputted current state be $s^t \in s_i^t, \dots, s_N^t$ (a $W \times H \times C$ matrix),
 311 where $W = 256$ and $H = 256$ are the weight and height, respectively, of that
 312 state, $W \times H$ is the number of pixels (i.e., $i = 1, \dots, N$), and $C = 3$ is the
 313 number of channels. The first step of the graph-driven context-aware agent
 314 module is the exploration of the local feature $F^t \in (F_i^t, \dots, F_N^t)$ for each pixel
 315 of that state by constructing two 5×5 FC convolutional layers, where F^t is
 316 also a matrix ($W \times H \times D$), and $D = 64$ is the number of feature dimen-
 317 sions. Then, the second step is the exploration of the long-range contextual
 318 features $Z^t \in (X_i^t, \dots, Z_N^t)$ based on the local feature F^t by building three
 319 5×5 graph convolution layers, where Z^t is a matrix ($W \times H \times R$, $R = 128$).
 320 This step has two inputs, namely, a graph structure built by taking F_i^t as the
 321 i -th node and an adjacency matrix A^t ($N \times N$ matrix) represented by the
 322 node relationship. Here, the adjacency matrix A^t is computed by combining
 323 the superpixel (SLIC algorithm (Achanta et al., 2012)) and Gaussian kernel
 324 function. This adjacency matrix considers not only the superpixel relation-
 325 ship between pixels in the current state but also the distance between pixels
 326 to effectively guide node feature aggregation during convolutional learning.
 327 For each node, the adjacency matrix A_i^t can be formulated as:

$$A_i^t = \mathcal{G}(i, i')^{\mathcal{S}(i)}, \quad (2)$$

328 where $\mathcal{G}(,)$ is the kernel distance of two pixels (i and i'), and $\mathcal{S}(i)$ is 1 (if i
 329 and i' have the same superpixel) or 0.5 (if i and i' have different superpixels).
 330 The size of the superpixels is (approximately) 8×8 .

331 3.1.2. Efficient State-behavior network-based candidate action estimation

332 The state-behavior network integrates the FC-graph convolutions with
 333 the policy softmax layer to estimate all possible pixel-level candidate actions

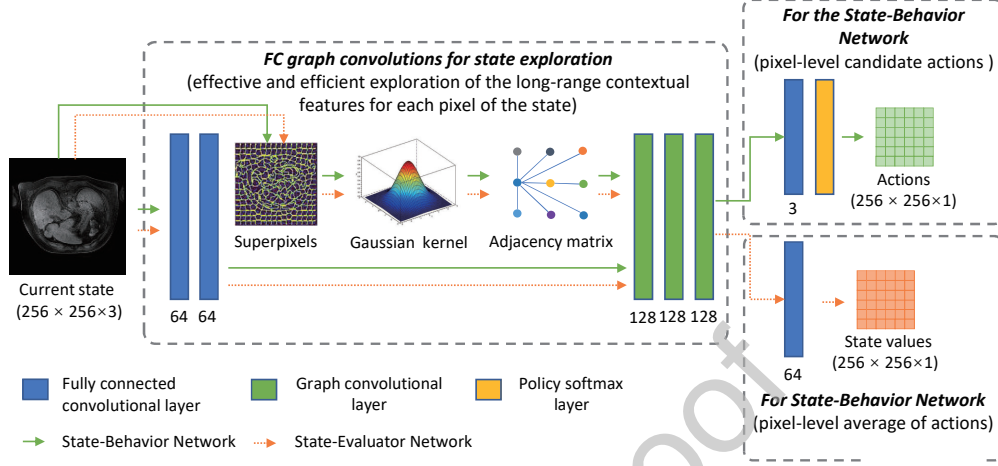


Figure 8: The state-behavior network leverages the FC graph convolutions with the policy softmax layer to improve the action estimation for each pixel of the current state. Additionally, the state-evaluator network leverages the FC graph convolutions with the regression layer to accurately predict the average actions for each pixel of the current state. Note that the adjacency matrix is computed by combining the superpixel relationship between pixels and the Gaussian kernel-based distance relationship, which can effectively guide the aggregation of the features during convolutional learning.

334 a^t for each pixel of the current state s^t based on the learned policy $\pi(a^t|s^t)$.
 335 It guides the pixel-level agents to accurately push the pixel intensity values
 336 of nonenhanced liver images to approach Gd-enhanced liver tumor images.
 337 Here, a^t is a 2D $W \times H$ matrix. Specifically, for pixel i , the network first
 338 uses the FC-graph convolutions to learn the features $Z(i)^t$ from the current
 339 state, followed by a 5×5 FC convolutional layer and a policy softmax layer to
 340 output a_i^t . a_i^t includes three types of pixel values: 1) increasing pixel values
 341 (pixel intensity $\times 1.05$); 2) decreasing pixel values (pixel intensity $\times 0.95$);
 342 and 3) constant pixel values (pixel intensity $\times 1.00$).

343 Furthermore, the policy softmax is based on the Gibbs softmax method,
 344 which can be expressed as:

$$\pi(a^t|s^t) = \Pr \{a^t = a|s^t = s\} = \frac{e^{p(s,a)}}{\sum_b e^{p(s,b)}}, \quad (3)$$

345 where $p(s, a)$ are the values of the modifiable policy parameters of the state-
 346 behavior network at time t , indicating the tendency to select (give preference
 347 to) each action a^t for each state s^t .

348 *3.1.3. Efficient state-evaluator network-based average action prediction*

349 The state-evaluator network embeds the FC-graph convolutions into a re-
 350 gression layer to predict the average pixel-level actions V_t for all the estimated
 351 actions (i.e., the expected total reward) for each pixel of the current state.
 352 It encourages the pixel-level agents to determine whether candidate actions
 353 have proceeded better or worse than expected. For pixel i , the network first
 354 uses the FC-graph convolutions to learn the features $Z(i)^t$ from the current
 355 state, followed by a 5×5 FC convolutional layer to directly regress V_i^t . The
 356 ground truth of the a set of values $V_t \in \{V_t^1 \dots V_t^N\}$ is the total expected
 357 reward $R_t \in \{R_t^1 \dots R_t^N\}$, which is computed by summing the present and
 358 historical rewards at that state. It can be defined as:

$$R^{(t)} = r^{(t)} + \gamma r^{(t+1)} + \gamma^2 r^{(t+2)} + \dots + \gamma^{n-1} r^{(t+n-1)} + \gamma^n V(s^{(t+n)}), \quad (4)$$

359 where r^t is the action reward by taking action a^t at state s^t

360 The **superiority** of our novel graph-driven context-aware agent module
 361 can be summarized as follows. 1) FC convolutions are integrated into graph
 362 convolutions to explore long-range contextual features for each pixel-level
 363 agent without interference between ambiguous local features. 2) All the
 364 agents are trained as a matrix convolution operation to share the weight of
 365 the representing parameters of actions and significantly reduce the agents'
 366 computational cost. 3) A fully connected network without any dimension
 367 reduction operation (pooling or stride) is used to ensure that no pixel features
 368 disappear and location information is confused when the iterative state is
 369 updated.

370 *3.2. Dual-level complementary reward based advantage function for pixel-*
 371 *level action optimization*

372 To enable the pixel-level agents to find the optimal actions, Pix-GRL
 373 integrates the advantage function (Mnih et al., 2016) with the dual-level
 374 complementary reward. The dual-level complementary reward is a measure-
 375 ment that improves each pixel value change before and after an action. The
 376 advantage function is a reward-based measurement that guides the agents to
 377 find which action is optimal for each pixel in the current state. By integrat-
 378 ing the dual-level complementary reward and the advantage function, the
 379 pixel-level agents take the optimal action to update the state and feed the

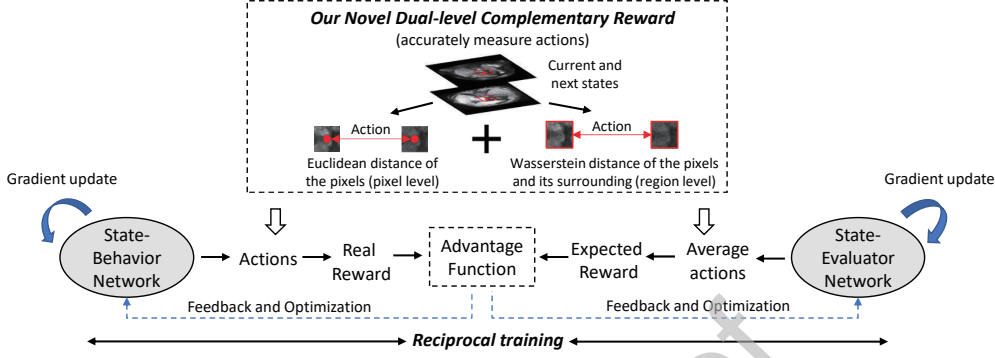


Figure 9: Both the state-behavior network and state-evaluator network leverage the advantage function to reciprocally train each other and improve training performance, thereby accurately finding the best actions to update the state.

380 parameters of that action back to the graph-driven context-aware agent module to reciprocally train the state-behavior network and the state-evaluator
 381 network.
 382

383 3.2.1. Dual-level complementary reward-based accurate action measurement

384 The dual-level complementary reward (Fig. 9) combines a pixel-level reward
 385 function with the Euclidean distance and a region-level reward function
 386 with the Wasserstein distance to improve the measurement accuracy. The
 387 reward ensures that each action considers not only each pixel with its own
 388 future state but also those of neighboring pixels and ensures that each agent
 389 is optimized in both the pixel and local context texture of the state. For each
 390 pixel i , the dual-level complementary reward r_i^t at state s^t can be formulated
 391 as follows:

$$r_i^t = \underbrace{r(e)_i^t}_{\text{Pixel-level reward}} + \lambda \underbrace{r(w)_i^t}_{\text{Region-level reward}}, \quad (5)$$

392 where $r(e)_i^t$ is the reward computed by the pixel-level reward function, and
 393 $r(w)_i^t$ is the reward computed by the region-level reward function.

394 **Euclidean distance-based pixel-level reward function.** The pixel
 395 reward function leverages the Euclidean distance to measure the improve-
 396 ment in every pixel value compared to each pixel in the current state and
 397 its own future state caused by that pixel’s action. This function is able to
 398 optimize each pixel with its pixel-level agent independently to improve the

399 effect of actions on the synthesis of pixel content details at each time state.
 400 This function can be formulated as follows:

401 This function can be formulated as follows:

$$\text{Pixel-level : } r(e)_i^t = \left((I_i^{\text{CA}} - s_i^{(t)})^2 - (I_i^{\text{CA}} - s_i^{(t+1)})^2 \right), \quad (6)$$

402 where I_i^{CA} are the Gd-enhanced liver tumor images.

403 **Wasserstein distance-based region-level reward function.** The region
 404 reward function leverages the Wasserstein distance (Vallender, 1974) to
 405 measure the improvement in each action for the corresponding pixel and sur-
 406 rounding pixels between the current state and future state. This function is
 407 able to optimize neighboring actions jointly to improve the synthesis of the
 408 general context at each time state and avoid the local optima from the local
 409 optimization of only the pixel-level reward function. We chose the Wasser-
 410 stein distance as the regional-level reward because of its two advantages. 1)
 411 Wasserstein distance is a symmetric distance metric. It can measure the dis-
 412 tance between a discrete distribution and a continuous distribution. Thus,
 413 it can better measure the distance between the distributions of different re-
 414 gions in states based on a disordered, random update (Yang et al., 2018).
 415 2) The Wasserstein distance includes geometric properties (Panaretos and
 416 Zemel, 2019). It measures the distance between two distribution transforms
 417 and presents the geometric characteristics of the distribution. Thus, it can
 418 leverage the geometric characteristics of the ground truth to guide pixel-level
 419 actions in order to optimize the regions during state updates.

$$\text{Region-level : } r(w)_i^t = \inf_{\gamma \in \Pi(\mathbb{P}_{H_i^t}, \mathbb{P}_{H_i^{t+1}})} \mathbb{E}_{(x,y) \sim \gamma} [\|x - y\|], \quad (7)$$

420 where H_i^t and H_i^{t+1} are 16×16 patches with pixel i as the centroid in the
 421 current state t and the next state $t + 1$. We managed the patch for the pixels
 422 at the edges of the image by zero padding. $\Pi(\mathbb{P}_{H_i^t}, \mathbb{P}_{H_i^{t+1}})$ denotes the set of
 423 all joint distributions $\gamma(x, y)$ whose marginals are $\mathbb{P}_{H_i^t}$ and $\mathbb{P}_{H_i^{t+1}}$. In other
 424 words, $\gamma(x, y)$ indicates how much “mass” must be transported from x to y
 425 to transform distribution $\mathbb{P}_{H_i^t}$ into distribution $\mathbb{P}_{H_i^{t+1}}$.

426 3.2.2. Finding the advantage function-based optimal action

427 The advantage function computes the extra rewards, which are the differ-
 428 ence between the real rewards (taking the candidate actions estimated from

429 the state-behavior network) and the expected rewards (the average actions
 430 predicted from the state-evaluator network). This function enhances a par-
 431 ticular action used to change the pixel values of a state to be better than
 432 the average actions in a given state, reducing the agent optimization vari-
 433 ability. The advantage function $A(a^{(t)}, s^{(t)})$ of action a^t at state $s^{(t)}$ can be
 434 formulated by:

$$A(a^{(t)}, s^{(t)}) = R^{(t)} - V(s^{(t)}). \quad (8)$$

435 This advantage function then takes feedback to update the parameters of
 436 the state-behavior network. Learning from this feedback, the state-behavior
 437 network learns what action is good for estimating a better action for each
 438 pixel at the next time point. It improves the action estimation performance
 439 from random estimation to accurate action output by the state understanding
 440 during iterative training. Let the parameters of the state-behavior network
 441 be denoted by θ_a . The state-behavior network can be updated by:

$$d\theta_a = -\nabla_{\theta_a} \log \pi(a^{(t)}|s^{(t)}) A(a^{(t)}, s^{(t)}). \quad (9)$$

442 If $A(a^{(t)}, s^{(t)})$ is positive, it suggests that the tendency to select a^t should be
 443 strengthened for the future, whereas if $A(a^{(t)}, s^{(t)})$ is negative, it suggests that
 444 the tendency should be weakened.

445 By the same token, this advantage function updates the parameters of
 446 the state-evaluator network. It helps the state-evaluator network to predict
 447 a more accurate expected reward in the next time point. Let the parameters
 448 of the state-evaluator network be denoted by θ_e , and the state-evaluator
 449 network can be updated by:

$$d\theta_e = \nabla_{\theta_e} (R^{(t)} - V(s^{(t)}))^2. \quad (10)$$

450 Thus, by combining Eq. 9 and Eq. 10, the objective function of the
 451 state-behavior network evaluator training of Pix-GRL is:

$$\nabla_{\theta} J(\theta) = \frac{1}{N} \sum_{i=1}^N \sum_{t=0}^T \nabla_{\theta_a} \underbrace{\log \pi_{\theta}(a_t|s_t)}_{\text{State-behavior network}} \nabla_{\theta_e} \underbrace{(Q(s_t, a_t) - V_{\phi}(s_t))}_{\text{State-evaluator network}}. \quad (11)$$

452 The **superiority** of the dual-level complementary reward can be sum-
 453 marized as follows. 1) Pixel-level actions are optimized with respect to both
 454 the pixel and the local content to avoid falling into local optima caused by
 455 focusing only on the actions of the individual pixel. 2) Wasserstein distance

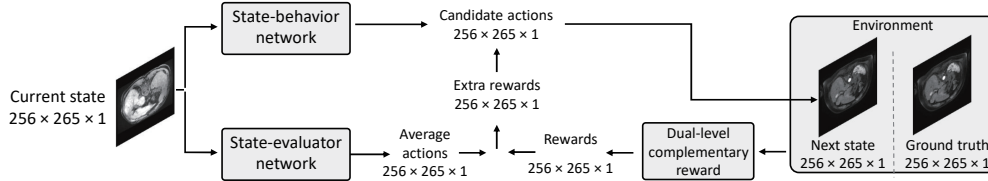


Figure 10: Our method consists of two networks and a reward function to obtain pixel-level actions for each pixel of the input image, i.e., the dimension of the input is the same as the dimension of the output in a state update.

456 is embedded into the reward computation to evaluate the geometric relation-
 457 ships between the state’s probability distributions to reduce distortions and
 458 the number of artifacts.

459 4. Experimental setup

460 4.1. Datasets

461 In total, 325 patients with liver axial MRI images were selected (100 pa-
 462 tients with hemangiomas, 150 patients with hepatocellular carcinoma and 75
 463 normal controls). The nonenhanced liver MRI images (T1-weighted gradient-
 464 recalled echo sequence) were obtained using a 1.5T MRI system (Signa
 465 Artist, GE Healthcare; Aera, Siemens healthcare). The slice thickness was 4
 466 mm, the matrix was 256×256 , and the pixel dimensions were 1.2882×1.2882 .
 467 The Gd-enhanced liver MRI images (T1-weighted fat-saturation imaging)
 468 were performed in the same orientations and with the same thickness, ma-
 469 trix, and pixel dimensions using a fat saturation sequence of 40 seconds to
 470 480 seconds after intravenous injection of a gadolinium-based contrast agent
 471 (0.1 mmol/kg).

472 4.2. Implementation

473 Pix-GRL uses 5-fold random cross-validation on three datasets for train-
 474 ing and testing. Our method processes 2D slices independently. The original
 475 data include an MR stack of images (36 slices – 120 slices). Both training
 476 and testing (evaluation) are carried out on multiple slices per patient. The
 477 average number of input slices is 62. It uses the chainer library to set the
 478 mini-batch number to 32 and uses the Adam optimizer (Kingma and Ba,
 479 2014) with a learning rate of 0.001. The maximum number of epochs is set
 480 to 80,000, Gamma is set to 0.15, and the length of each epoch is set to $50 \cdot \lambda$

481 is set to 0.15. It required 67 hours for training and 0.49 seconds on average
 482 for evaluating a test image whose size is 256×256 on 4 Tesla P100 GPUs. A
 483 nonrigid registration (Elastix, Erasmus, Netherlands) was used as a prepro-
 484 cessing step to register Gd-enhanced liver MR images to the corresponding
 485 nonenhanced liver MR images. This registration prevents the potential mis-
 486 alignment caused by the slight slice error and motion artifacts during imaging
 487 and keeps this misalignment from affecting synthesis performance.

488 4.3. Workflow section

489 As shown in the above 10, our method consists of two networks and a
 490 reward function to obtain pixel-level actions for each pixel of the input image,
 491 i.e., the dimension of the input is the same as the dimension of the output
 492 in a state update. 1) A state-behavior network. Input: the current state,
 493 $256 \times 256 \times 1$ (where 256×256 are the height and width of each image, and
 494 1 is the number of channels). The initial current state is the nonenhanced
 495 liver image. Output: candidate actions, $256 \times 256 \times 1$. 2) A state-evaluator
 496 network. Input: the current state, $256 \times 256 \times 1$. Output: average actions
 497 (i.e., expected rewards), $256 \times 256 \times 1$. 3) A dual-level complementary reward.
 498 Input: Gd-enhanced liver image, $256 \times 256 \times 1$, and next state, $256 \times 256 \times 1$
 499 (taking candidate actions). Output: rewards (i.e., pixel level), $256 \times 256 \times 1$.

500 These three types of outputs are collaborative. They compute the extra
 501 rewards to find the optimal action in the current state by comparing the
 502 rewards and the expected rewards (the average actions). They also measure
 503 all actions to optimize two networks to achieve better candidate actions and
 504 better average actions in the next state.

505 4.4. Evaluation metrics

506 The performance of Pix-GRL is evaluated in three aspects:

- 507 • the experiments will prove that AI-enhanced liver tumor images can
 508 achieve high image quality when compared to Gd-enhanced liver tu-
 509 mor images by image similarity metrics. The network compares these
 510 two types of images in the overall image by calculating the structural
 511 similarity index (SSIM), peak signal-to-noise ratio (PSNR), and nor-
 512 malized root-mean-square error (NRMSE). Moreover, after two experi-
 513 enced radiologists manually segmented the tumors from them, the net-
 514 work compares these two types of images in diagnostic detail (internal:
 515 tumor’s minimum bounding box; external: 64×64 patch including

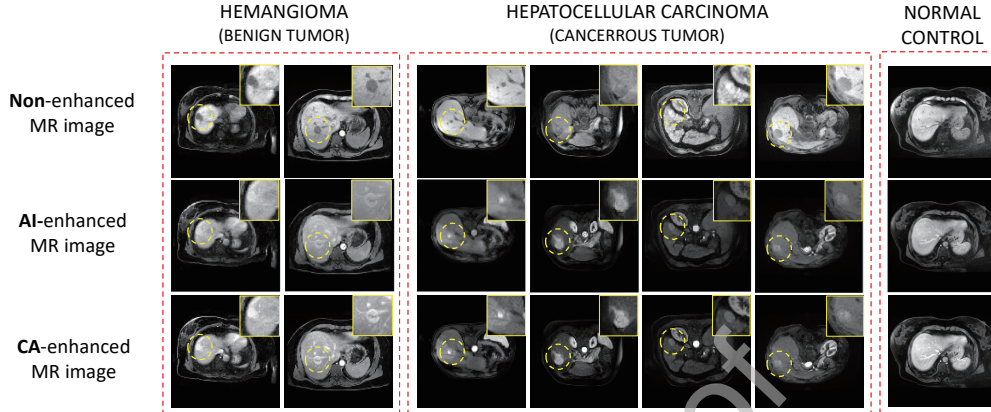


Figure 11: Visual examples prove that Pix-GRL can produce high-quality AI-enhanced liver tumor images of all benign liver tumors, cancerous tumors, and normal controls compared with the Gd-enhanced liver tumor images. Note that the tumors are marked by yellow dotted circles.

516 tumors) by calculating the normalization mutual information (NMI),
 517 PSNR, and NRMSE.

- 518 • The experiments will prove that AI-enhanced liver tumor images can
 519 provide accurate manual tumor segmentation results (i.e., location,
 520 shape, and size) in the clinical workflow when compared to the Gd-
 521 enhanced liver tumor images by segmentation metrics. After the two
 522 types of tumors have been manually segmented by radiologists, the net-
 523 work compares these two types of segmented tumors by calculating the
 524 Dice coefficient, the kappa coefficient, and the Hausdorff distance.
- 525 • The experiments will prove that AI-enhanced liver tumor images can
 526 provide accurate tumor diagnoses compared to Gd-enhanced liver tu-
 527 mor images by clinical metrics. After the two experienced radiologists
 528 diagnosed the tumors based on the two types of images, including the
 529 nonenhanced liver images, the network calculated the Pearson correla-
 530 tion coefficient (PCC) for the tumor sizes, the accuracy of benign and
 531 cancer tumor diagnosis (binary classification), and the average accuracy
 532 of tumor staging (LI-RADS 2-5, 4 categories classification).

Table 1: Pix-GRL achieved not only high image quality but also accurate diagnostic detail in the AI-enhanced MR images.

High overall image quality		
SSIM	NRMSE	PSNR
0.85 ± 0.06	0.16 ± 0.012	23.81 ± 1.54
High diagnostic detail of the tumor (external)		
SSIM	NRMSE	NMI
0.81 ± 0.06	0.11 ± 0.01	0.61 ± 0.07
High diagnostic detail of the tumor (internal)		
SSIM	NRMSE	NMI
0.72 ± 0.08	0.07 ± 0.009	0.43 ± 0.05

533 5. Experimental Results

534 Comprehensive experiments indicated that Pix-GRL produces high-quality
 535 AI-enhanced liver tumor images. Pix-GRL achieved an SSIM of 0.85 for the
 536 overall image, an NRMSE of 0.16 for the overall image, a Dice coefficient
 537 of 0.83 of the manual tumor segmentation, an accuracy of 87.60% of tumor
 538 diagnosis (benign or cancerous). These results demonstrate that Pix-GRL
 539 has great potential to become an accurate clinical alternative to eliminate
 540 the use of CA in liver tumor imaging.

541 5.1. The high image quality of the AI-enhanced liver tumor images

542 Fig. 11 and Fig. 12 indicate that Pix-GRL was successful in produc-
 543 ing high-quality AI-enhanced liver tumor images, which were almost visually
 544 identical to the Gd-enhanced liver tumor images. Moreover, Table. 1 indi-
 545 cates that the AI-enhanced liver tumor images from Pix-GRL achieved high
 546 performance in the image quality metrics.

547 **Overall image quality.** Pix-GRL achieved a high overall image quality
 548 for the AI-enhanced MR images when compared to the Gd-enhanced MR
 549 images, achieving an SSIM of 0.85 ± 0.06 , a PSNR of 23.81 ± 1.54 , and an
 550 NRMSE of 0.16 ± 0.012 .

551 **Internal tumor diagnostic details.** Pix-GRL provided high internal
 552 tumor diagnostic details when comparing the AI-enhanced liver tumor im-
 553 ages and the Gd-enhanced liver tumor images. The radiologists first manu-
 554 ally segmented the tumors from the Gd-enhanced liver tumor images, and the
 555 minimum bounding box of each tumor was calculated and cropped. Then,

556 according to the location of these minimum bounding boxes, the minimum
 557 bounding boxes of the tumors in the AI-enhanced MR images can be calcu-
 558 lated and cropped. Pix-GRL achieved an SSIM of 0.72 ± 0.08 , an NRMSE of
 559 0.07 ± 0.009 , and an NMI of 0.43 ± 0.05 when comparing these two types of
 560 minimum bounding boxes of segmented tumors.

561 **External tumor diagnostic details.** Pix-GRL provided high external
 562 tumor diagnostic details when comparing the surrounding pixels of the tu-
 563 mors from the AI-enhanced liver tumor images and the Gd-enhanced liver tu-
 564 mor images. After the tumors are manually segmented from the Gd-enhanced
 565 liver tumor images, the centroid of each tumor is calculated, and 64×64
 566 tumor patches including the tumors are cropped in the two types of images .
 567 The Pix-GRL achieved an SSIM of 0.81 ± 0.06 , an NRMSE of 0.11 ± 0.01 , and
 568 an NMI of 0.61 ± 0.07 when comparing these two types of tumor patches.

569 Note that higher values for the SSIM, PSNR, and NMI and lower values
 570 for the NRMSE indicate better performance.

571 *5.2. Accurate manual tumor segmentation in the AI-enhanced liver tumor* 572 *images*

573 Table 2 also shows that the AI-enhanced liver tumor images of Pix-GRL
 574 provided accurate manual tumor segmentation (i.e., location, shape, and size
 575 of tumors of the manually segmented tumors) compared to the tumors in the
 576 Gd-enhanced liver tumor images. After the two types of tumors are manually
 577 segmented, two types of tumor binary images can be obtained by setting all
 578 the pixels of the tumor to 0 and the remaining pixels to 255. As shown by the
 579 binary versions of the Gd-enhanced liver tumor images as the ground truth,
 580 Pix-GRL achieved a Dice coefficient of $83.62\% \pm 6.28\%$, a kappa coefficient
 581 of 0.83 ± 0.06 , and a Hausdorff distance of $4.3 \text{ mm} \pm 1.02 \text{ mm}$ in the two
 582 types of tumor binary images. Note that higher values for the Dice and
 583 kappa coefficients and lower values for the Hausdorff distance indicate better
 584 performance.

585 *5.3. Comparable tumor diagnosis of the AI-enhanced liver tumor images and* 586 *Gd-enhanced liver tumor images*

587 Table 2 shows that the AI-enhanced MR image from Pix-GRL provided
 588 tumor diagnosis results comparable to those of the radiologists compared to
 589 the Gd-enhanced liver tumor images from current clinical workflows. After

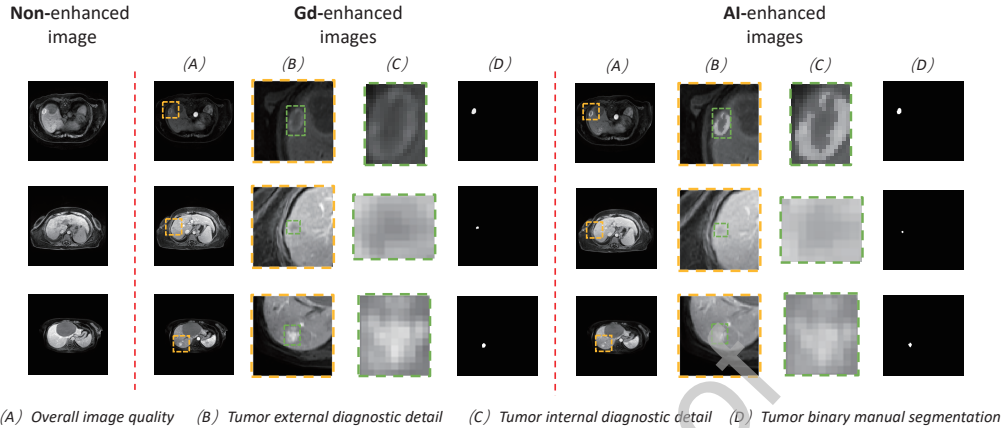


Figure 12: Compared with the Gd-enhanced liver tumor images, Pix-GRL produces high-quality AI-enhanced liver tumor images in the overall image, external diagnostic details of the tumor, internal diagnostic details of the tumor, and manual tumor segmentation.

590 the radiologists analyzed these two types of images (including the nonen-
 591 hanced liver images), and the analysis results of the Gd-enhanced liver tu-
 592 mor images were taken as the ground truth, Pix-GRL achieved a PCC for
 593 the tumor size of 0.92 (44.54 ± 39.77 mm for the AI-enhanced MR images vs.
 594 48.59 ± 38.59 mm for the nonenhanced liver images, $P=0.19$), as shown in
 595 Fig. 13. Moreover, Pix-GRL achieved a tumor diagnosis accuracy (binary
 596 classification of benign or cancerous) of 87.60%, a sensitivity of 81.65%, and
 597 a specificity of 92.20%. Additionally, Pix-GRL achieved an average accu-
 598 racy of clinic liver cancer staging (four-category classification of LI-RADS
 599 2-5) of 80.66%, an average sensitivity of 73.84%, and an average specificity
 600 of 87.21%. Specifically, the classification accuracy of LI-RADS 2 is 67.71%,
 601 that of LI-RADS 3 is 90.07%, that of LI-RADS 4 is 88.14%, and that of
 602 LI-RADS 5 is 81.11%. The ROC curves of these classifications are shown in
 603 Fig. 13.

604 5.4. Advantage of DRL in AI-enhanced liver image synthesis

605 Figs. 15 and 14 indicate that Pix-GRL produced better tumor diagnostic
 606 details than the existing image-to-image synthesis frameworks. Compared to
 607 Pix2Pix (Isola et al., 2017), PLDT (Yoo et al., 2016), and U-net (Ronneberger
 608 et al., 2015) (here, all of these compared methods are trained by using the
 609 default network structure and parameters listed in their references), Pix-GRL
 610 improved the SSIM by 0.01-0.13 and the NRMSE by 0.03-0.14 in terms of the

Table 2: Pix-GRL achieved not only high image quality but also accurate diagnosis values in the AI-enhanced MR images.

Accurate manual tumor segmentation		
Dice coefficient	Kappa coefficient	Hausdorff distance
83.62% \pm 6.28%	0.83 \pm 0.06	4.3 mm \pm 1.02mm
Comparable tumor diagnosis (AI- vs. Gd-enhanced liver tumor image)		
PCC for the tumor size	Accuracy of tumors diagnosis (benign or cancerous))	Average accuracy of cancer staging (LI-RADS 2-5)
0.92	87.60%	80.66%

611 overall image quality. It improved the SSIM by 0.01-0.17 and the NRMSE by
 612 0.03-0.14 in the external diagnostic details of the tumors. It also improved
 613 the SSIM by 0.01-0.16 and the NRMSE by 0.03-0.14 in the internal diagnostic
 614 details of the tumors. Moreover, Pix-GRL produced more accurate tumor
 615 segmentation metrics and tumor diagnosis results than these methods. It
 616 improved the Dice coefficient by 0.01-0.13 and the kappa coefficient by 0.02-
 617 0.10 in manual tumor segmentation. It also improved the PCC for the tumor
 618 size by 0.01-0.13 and the accuracy of tumor diagnosis (benign or cancerous) by
 619 0.04-0.017. All these improvements are because Pix-GRL uses the powerful
 620 feature dynamic self-learning ability of DRL to optimize each pixel separately.
 621 It can use the Gd-enhanced images to guide the self-learning pixel-level agents
 622 to iteratively understand the intrinsic features of the tumors, compared to the
 623 traditional deep learning methods, which use a one-time mapping between
 624 the AI-enhanced liver tumor images and Gd-enhanced liver tumor images.
 625 Thus, it is able to explore all possibilities to learn the optimal actions for
 626 synthesis in a wider feature space, avoiding inaccurate mapping caused by
 627 suboptimal optimization or overfitting. Furthermore, Pix-GRL uses a graph-
 628 driven context-aware agent module with dual-level complementary rewards
 629 to optimize the task in terms of both local and global optimization. It avoids
 630 GAN-based methods and overall image distribution distance optimization,
 631 avoids focusing only on those details that make a greater contribution to
 632 reduce the distance and ignores small diagnostic details. Fig. 17 shows
 633 that Pix-GRL improved the image quality compared to some state-of-the-art
 634 image-to-image synthesis frameworks.

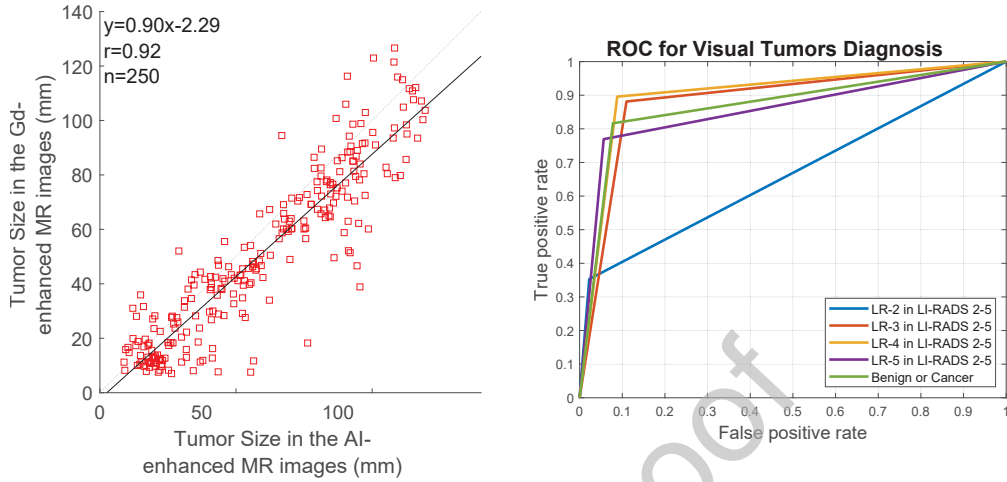


Figure 13: The AI-enhanced MR images from Pix-GRL provided tumor diagnoses comparable to those of the radiologists compared to the Gd-enhanced MR images of the current clinical workflows. A Pearson correlation coefficient of 0.92 was achieved in terms of the tumor size. Additionally, Pix-GRL achieved a tumor diagnosis accuracy (binary classification of benign or cancerous) of 87.60% and an average accuracy of clinical liver cancer staging (four-category classification of LI-RADS 2-5) of 80.66%.

635 5.5. Superiority of the advantage function-based optimal action training

636 Figs. 15 and 14 indicate that using the advantage function reciprocal
 637 training state-behavior network and the state-evaluator network achieved
 638 a better performance than existing DRL methods in finding the optimal
 639 action for image synthesis. Comparing the famous policy gradient (Monte-
 640 Carlo policy gradient) algorithm (Babaeizadeh et al., 2016) (trained using the
 641 graph-driven context-aware agent module and unchanged global parameters)
 642 and the value-based DQN algorithm (Babaeizadeh et al., 2016) (trained using
 643 the graph-driven context-aware agent module and unchanged global param-
 644 eters), Pix-GRL improved the SSIM by 0.03-0.06, 0.03-0.05 and 0.02-0.07 in
 645 terms of the overall image quality, internal diagnostic details of the tumors,
 646 and external diagnostic details of the tumors, respectively. It improved the
 647 Dice coefficient by 0.02-0.08 and the kappa coefficient by 0.03-0.08 in terms
 648 of manual tumor segmentation. It also improved the PCC for the tumor
 649 size by 0.04-0.08 and the tumor diagnosis accuracy (benign or cancerous) by
 650 0.06-0.11. All these improvements occur because Pix-GRL uses an advantage
 651 function to integrate a value-based algorithm and a policy-based algorithm,
 652 thereby exploiting their advantages while eliminating all their drawbacks.

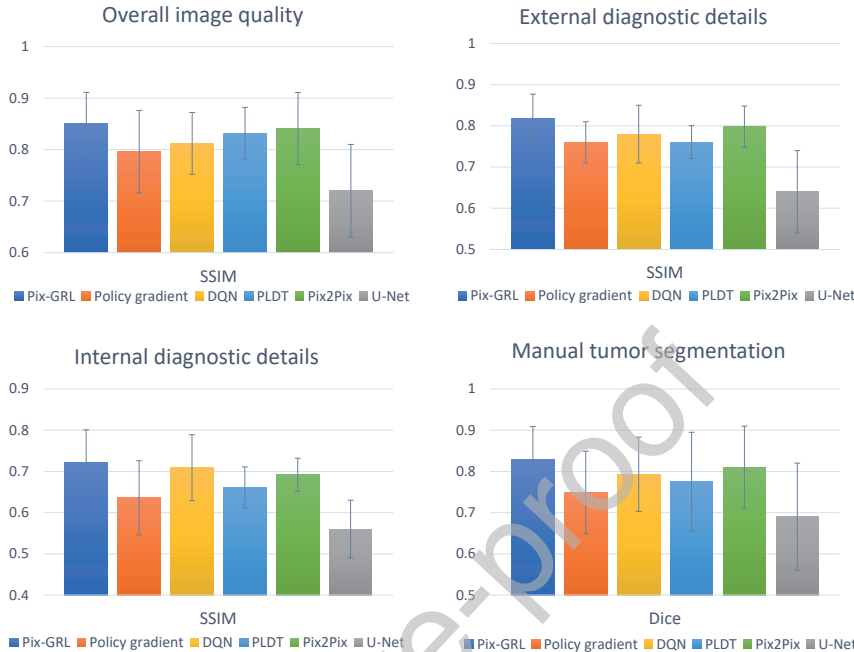


Figure 14: Pix-GRL produced better AI-enhanced liver tumor images than the existing image-to-image synthesis frameworks, namely, Pix2Pix, PLDT, and U-Net. Moreover, Pix-GRL outperforms existing DRL methods, namely, the policy-based policy gradient algorithm and the value-based DQN algorithm, in medical image synthesis.

653 It is able to use the state-behavior network to control the agent’s behavior
 654 by learning the optimal policy (policy-based algorithm) and uses the state-
 655 evaluator network to evaluate the action by computing the value function
 656 (value-based algorithm). These two models participate in a game where they
 657 both improve in their own role over time. The result is that the overall archi-
 658 tecture will learn to play the game more efficiently than the two separate
 659 methods.

660 5.6. Advantage of the graph-driven context-aware agent module

661 Table 3 indicates that our graph-driven context-aware agent module en-
 662 ables Pix-GRL to produce better AI-enhanced liver tumor images than other
 663 network structures. We use FCN-8s, U-Net, ResNet-18 (removing the last
 664 pooling layer and softmax layer), 5 3×3 dilated convolution layers (called
 665 Dilated-CNN here, a dilation state-behavior network of [1, 2, 3, 2, 1] and a
 666 filter size of 128), and 5 2D 3×3 convolutional layers (called CNN here with

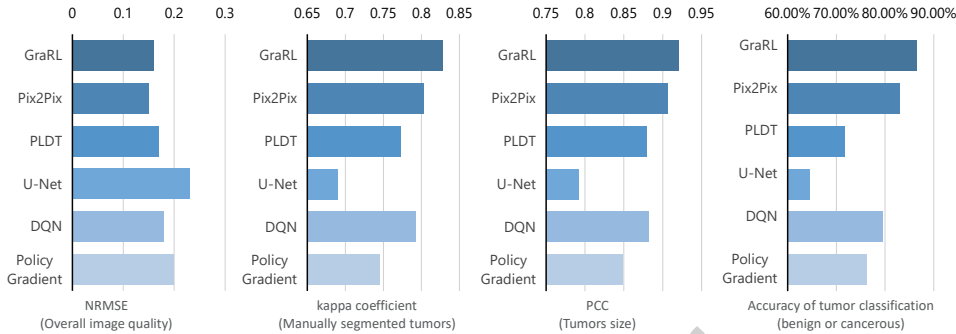


Figure 15: Pix-GRL produced better tumor diagnostic details than the existing image-to-image synthesis frameworks including Pix2Pix, PLDT, and U-net in terms of the kappa coefficient, the PCC of tumors sizes, and the accuracy of benign and cancer tumors diagnosis. Moreover, Pix-GRL outperforms existing DRL methods including policy-based policy gradient algorithm and the value-based DQN algorithm in these terms.

667 a filter size of 128) to build the state-behavior network and state-evaluator
 668 network to evaluate the graph-driven context-aware agent module. Here, the
 669 batch normalization layers of all the compared network structures were re-
 670 moved, followed by the policy softmax and the fully connected convolution
 671 layers (filter size of 1) to output the actions and state values, respectively.
 672 By comparison, the graph-driven context-aware agent module improved the
 673 SSIM by 0.2-0.8 in terms of the overall image quality. It improved the Dice
 674 coefficient by 2.14%-4.45% in terms of the manual tumor segmentation. Ad-
 675 ditionally, it improved the PCC by 0.2-0.4 in terms of the tumor size. All
 676 of these improvements are achieved because the graph-driven context-aware

Table 3: Our graph-driven context-aware agent module models the pixel-level agents better than the current state-of-the-art deep learning network structure and explores the current state to generate better AI-enhanced liver tumor images in terms of the image quality, tumor segmentation, and tumor size.

	Graph-driven FCN-8s	U-Net	ResNet-18	Dilated-CNN	CNN	
SSIM (Overall)	0.85	0.80	0.81	0.82	0.83	0.77
Dice (Segmentation)	83.62%	79.51%	79.17%	80.05%	81.20%	80.14%
PCC (Tumor size)	0.92	0.89	0.88	0.90	0.90	0.88

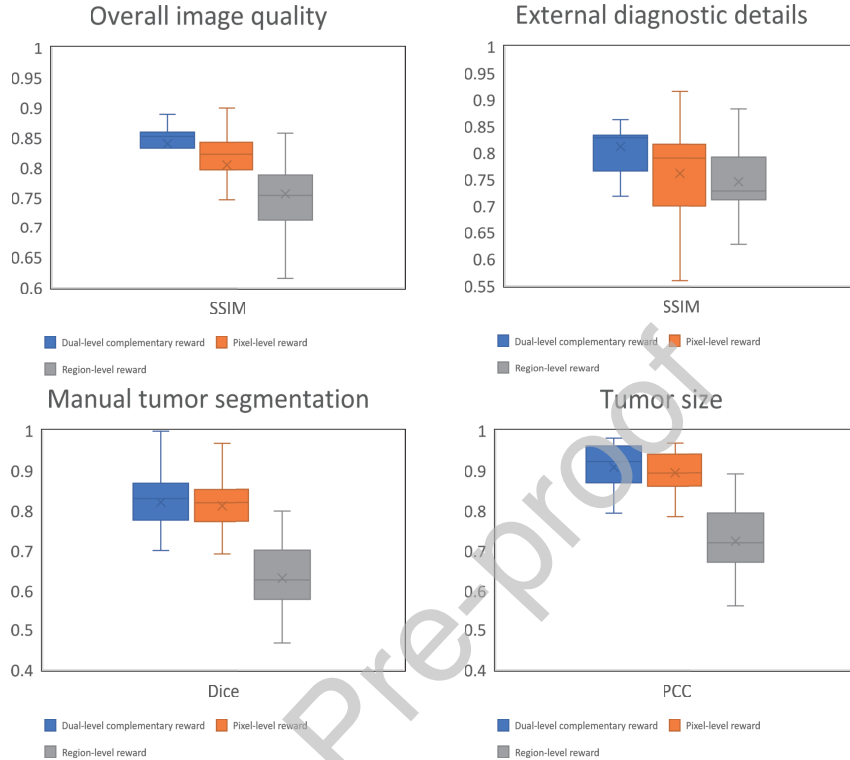


Figure 16: The dual-level complementary reward that combines the pixel-level reward and the region-level reward produces better AI-enhanced liver tumor images in terms of the overall image, external diagnostic details of the tumors, internal diagnostic details of the tumors, and manual tumor segmentation than the single pixel-level reward and region-level reward.

677 agent module efficiently embeds the relationships between pixels into pixel-
 678 level agents to capture long-range contextual features rather than a pure
 679 convolutional layer stacked with local features. The module avoids confusion
 680 and loss of contextual information between adjacent pixel-level agent rep-
 681 resentation learning caused by the pooling layers and downsampling in the
 682 FCN-8s, U-Net, and ResNet-18 models, thereby presenting more accurate
 683 image details. It also prevents the well-known grid effect and the insensitiv-
 684 ity of the small objects in the dilated convolution, thereby improving tumor
 685 synthesis.

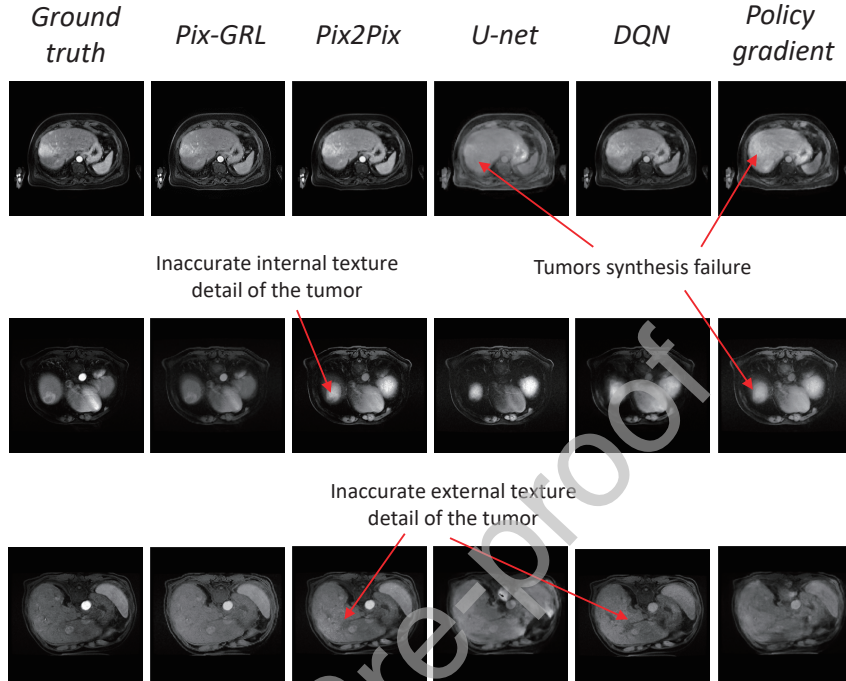


Figure 17: Pix-GRL produced better AI-enhanced liver tumor images than the existing image-to-image synthesis frameworks: Pix2Pix, U-Net, and policy gradient algorithm and DQN.

686 5.7. Advantage of the dual-level complementary reward

687 Fig. 16 indicates that the dual-level complementary reward improved the
 688 performance of Pix-GRL. Comparing the use of the single pixel-level reward
 689 and the single region-level reward, the pixel-region reward improved the SSIM
 690 by 0.04-0.10 in terms of the overall image quality, the SSIM by 0.03-0.06 in
 691 terms of the external diagnostic details, the Dice coefficient by 1.86%-19.07%
 692 in terms of manual tumor segmentation, and the PCC by 0.1-0.20 in terms of
 693 the tumor size. The reason is because the dual-level complementary reward
 694 endows each agent to consider not only the future states of its own pixel
 695 but also those of the neighboring pixels. It ensures that both local content
 696 details of each pixel and the global texture details of a region can be effi-
 697 ciently learned to facilitate action generation of Pix-GRL. Moreover, it also
 698 improves the smoothness of the AI-enhanced liver tumor images, avoiding de-
 699 fective pixels and artifacts caused by independent suboptimal optimization

700 from each pixel based on only the pixel-level reward. Furthermore, a compar-
 701 ison of Wasserstein distance with KL divergence, MSE, and Jensen-Shannon
 702 divergence to performance has been performed. The comparison results indi-
 703 cate that the Wasserstein distance improves 0.01-0.03 by SSIM (internal
 704 diagnostic detail) and 0.01-0.03 by the Dice coefficient (manual segmenta-
 705 tion). All these improvements demonstrate the advantage of Wasserstein
 706 distance to measure regional reward.

707 *5.8. Comparison with one related work (Zhao et al., 2020)*

708 Pix-GRL is the first network to be applied in AI-enhanced liver tumor
 709 image synthesis, producing a higher-quality image and diagnosis accuracy
 710 than one related method (Zhao et al., 2020). Note that this related method
 711 (Zhao et al., 2020) is a tumor segmentation method, and synthesized rough
 712 enhanced images are just an intermedia auxiliary for tumor segmentation.
 713 As shown in Table 4, Pix-GRL improved the SSIM by 0.21 in terms of the
 714 internal diagnostic details and the SSIM by 0.07 in terms of the external
 715 diagnostic details. Pix-GRL improved the Dice coefficient by 0.02 in terms
 716 of manual tumor segmentation, the PCC by 0.06 in terms of the tumor
 717 size, and the accuracy by 0.30 in terms of tumor diagnosis (benign or can-
 718 cerous). All of these improvements are because the Pix-GRL enables the
 719 high-quality synthesis of all the diagnostic details and uses them to achieve

Table 4: Pix-GRL is the first network designed for AI-enhanced liver tumor image synthesis and outperforms related work (Zhao et al., 2020). Note that this related method is a tumor segmentation method, and synthesized rough enhanced images are an intermediate auxiliary method for tumor segmentation.

	Our Pix-GRL method	(Zhao et al., 2020)
SSIM (external diagnostic detail)	0.81	0.74
SSIM (internal diagnostic detail)	0.72	0.51
Dice coefficient (manual segmentation)	0.83	0.80
PCC (tumor size)	0.92	0.86
Accuracy (tumor diagnosis)	0.87	0.57

Table 5: Pix-GRL produced the best performance by tuning the main network parameters, including the size of the action, the number of actions, the image-patch size in the region-level reward, and the λ value in the pixel-region action reward.

Differents size of actions						
	$\times\pm 1.5$	$\times\pm 1.2$	$\times\pm 1.1$	$\times\pm 1.07$	$\times\pm 1.05$	$\times\pm 1.01$
SSIM	0.69	0.76	0.75	0.80	0.85	0.55
Differents number of actions						
	$[\times\pm 1.05, \times 0]$	$[\times\pm 1.1, \times\pm 1.05, \times 0]$	$[\times\pm 1.5, \times\pm 1.1, \times\pm 1.05, \times 0]$			
SSIM	0.85	0.78	0.76			
Different λ value in the pixel-region action rewards						
	1.5	1	0.5	0.2	0.1	0.05
SSIM	0.77	0.77	0.78	0.85	0.84	0.82
Different image-patch size in the region-level reward						
	2×2	4×4	8×8	16×16	32×32	64×64
SSIM	0.80	0.80	0.84	0.85	0.82	0.83

720 accurate qualification metrics, as well as obtaining credible diagnoses, rather
721 than an intermediate auxiliary method focusing only on the tumor structural
722 information for binary segmentation.

723 5.9. Optimal training parameters

724 Table 5 indicates that Pix-GRL achieved the best performance by tuning
725 the main network parameters, including the size of the action, the number
726 of actions, the image-patch size in the region-level reward, and the λ value
727 in the pixel-region action reward. Comparing the different action sizes, in-
728 cluding $[\times\pm 1.5, \times\pm 1.2, \times\pm 1.1, \times\pm 1.05, \times\pm 1.01]$, using a range of $\times\pm 1.05$
729 to change the pixel value achieved the best overall image quality and im-
730 proved the SSIM by 0.5-0.16. Additionally, comparing the different numbers
731 of actions, including the 3 numbers of $[\times\pm 1.05, \times 0]$, 5 numbers of $[\times\pm 1.1,$
732 $\times\pm 1.05, \times 0]$, 7 numbers of $[\times\pm 1.5, \times\pm 1.1, \times\pm 1.05, \times 0]$, and 3 numbers
733 achieved the best overall image quality and improved the SSIM by 0.7-0.9.
734 The results indicate that more actions cannot achieve more accurate synthe-
735 sis. The reason is because searching for an optimal action from a matrix
736 $(256 \times 256)^7$ is too complex, which leads to a high searching error and high
737 computational cost, despite a reduction in the training time. Moreover, when
738 comparing the different λ values $[0.05, 0.1, 0.2, 0.3, 0.5, 1, 1.5]$, setting λ to

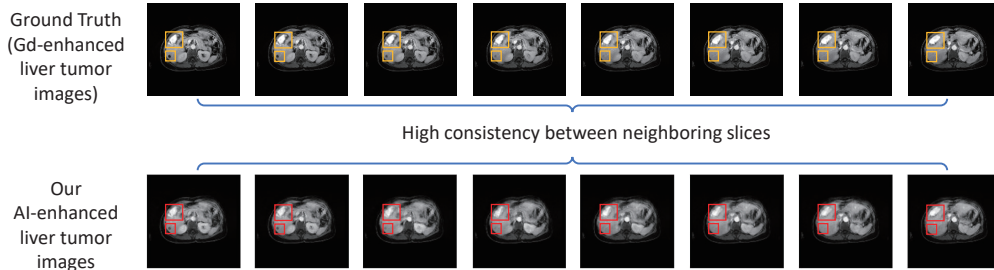


Figure 18: Visual example proving the high consistency between neighboring slices.

739 0.2 achieved the best overall image quality and improved the SSIM by 0.1-
 740 0.7. The reason is because the greater λ values lead the pixel agents to
 741 focus more on the region distance change between the current state and the
 742 next state, which smooths out the image details. The reason for setting the
 743 image-patch size as 16×16 is that this setting achieved the best performance.
 744 Compared to other sizes, including 2×2 , 4×4 , 8×8 , 32×32 , and 64×64 , the
 745 size of 16×16 improved the SSIM by 0.01 - 0.04. This improvement is because
 746 an excessively small patch lacks region distribution and causes the Wasser-
 747 stein distance to be similar to Euclidean distance, while an excessively large
 748 patch requires more overall optimization and causes the Wasserstein distance
 749 to perform poorly on pixel details. Moreover, Fig. 18 illustrates the consis-
 750 tency between neighboring slices (this patient includes 92 slices, but due to
 751 space limitations, we present only slices 40-47, which include tumors). This
 752 consistency strengthens the claims that our Pix-GRL does not invent non-
 753 existing lesions or tissues.

754 5.10. Limitations and further directions

755 As a pioneer work, our Pix-GRL still has several limitations: 1) Only a
 756 single-modality MR image is used as input for image synthesis. Our method
 757 uses only the single T1WI MR nonenhanced images as the inputted initial
 758 state for iterative updating. Although single nonenhanced T1WI MR im-
 759 ages are sufficient to achieve convincing results and prove the potential and
 760 feasibility of the method, integrating a wider variety of modalities in the
 761 input may improve the performance. Thus, in the future, we will use multi-
 762 modal images (such as T2WI and DWI) as the input to improve the efficiency
 763 and effectiveness of our method. 2) Our method has a high computational
 764 cost. Pix-GRL, as a DRL architecture, inevitably requires a large amount of

765 memory and a time-consuming training process. Although integrating graph
766 convolution in a fully connected network successfully reduced the substantial
767 cost of enabling pixel-level agent training, the cost caused by graph convolu-
768 tion in high-resolution images and fully connected matrix computation still
769 caused our method to require $4 \times$ NVIDIA 4 Tesla P100 GPU cards and
770 approximately 4 days for training. In the future, we plan to adapt recent
771 model compression technology to reduce the computational cost and improve
772 effectiveness while maintaining accuracy.

773 6. Conclusion

774 For the first time, a pixel-level graph reinforcement learning network was
775 used as a successful Gd-free imaging technology to generate output compara-
776 ble to Gd-enhanced liver tumor imaging. Pix-GRL was run using data from
777 325 subjects and yielded an SSIM of 0.85 for the AI-enhanced liver tumor
778 images, a Dice coefficient of 83.62% for manual tumor segmentation, and a
779 tumor diagnosis (benign and cancerous) accuracy of 87.60%. These results
780 demonstrate that Pix-GRL has great potential as an efficient and accurate
781 clinical tool for the standardization of liver tumor diagnosis and can avoid
782 all of the emerging toxicity concerns associated with CAs.

783 7. CRediT author statement

784 **Chenchu Xu:** Conceptualization, Methodology, Software, Writing -
785 Original Draft, Writing - Review and Editing. **Dong Zhang:** Conceptual-
786 ization, Methodology, Validation, Writing - Review and Editing. **Bo Chen:**
787 Data curation, Supervision, Visualization, Investigation, Writing- Review-
788 ing and Editing. **Shuo Li:** Supervision, Project administration, Software,
789 Writing- Reviewing and Editing.

790 References

791 Abubakar, I., Tillmann, T., Banerjee, A., 2015. Global, regional, and national
792 age-sex specific all-cause and cause-specific mortality for 240 causes of
793 death, 1990-2013: a systematic analysis for the global burden of disease
794 study 2013. *Lancet* 385, 117–171.

- 795 Achanta, R., Shaji, A., Smith, K., Lucchi, A., Fua, P., Süsstrunk, S., 2012.
796 Slic superpixels compared to state-of-the-art superpixel methods. *IEEE*
797 *transactions on pattern analysis and machine intelligence* 34, 2274–2282.
- 798 Alansary, A., Oktay, O., Li, Y., Le Folgoc, L., Hou, B., Vaillant, G., Kam-
799 nitsas, K., Vlontzos, A., Glocker, B., Kainz, B., et al., 2019. Evaluating
800 reinforcement learning agents for anatomical landmark detection. *Medical*
801 *image analysis* 53, 156–164.
- 802 Arora, S., Risteski, A., Zhang, Y., 2017. Theoretical limitations of encoder-
803 decoder gan architectures. *arXiv preprint arXiv:1711.02651* .
- 804 Babaeizadeh, M., Frosio, I., Tyree, S., Clemons, J., Kautz, J., 2016. Rein-
805 forcement learning through asynchronous advantage actor-critic on a gpu.
806 *arXiv preprint arXiv:1611.06256* .
- 807 Budak, Ü., Guo, Y., Tanyildizi, E., Şengür, A., 2020. Cascaded deep convo-
808 lutional encoder-decoder neural networks for efficient liver tumor segmen-
809 tation. *Medical hypotheses* 134, 109431.
- 810 Cano-Espinosa, C., González, G., Washko, G.R., Cazorla, M., Estépar,
811 R.S.J., 2020. Biomarker localization from deep learning regression net-
812 works. *IEEE Transactions on Medical Imaging* 39, 2121–2132.
- 813 Choi, Y., Choi, M., Kim, M., Ha, J.W., Kim, S., Choo, J., 2018. Stargan:
814 Unified generative adversarial networks for multi-domain image-to-image
815 translation, in: *Proceedings of the IEEE conference on computer vision*
816 *and pattern recognition*, pp. 8789–8797.
- 817 Cordts, M., Omran, M., Ramos, S., Rehfeld, T., Enzweiler, M., Benenson, R.,
818 Franke, U., Roth, S., Schiele, B., 2016. The cityscapes dataset for semantic
819 urban scene understanding, in: *Proceedings of the IEEE conference on*
820 *computer vision and pattern recognition*, pp. 3213–3223.
- 821 Duseja, A., 2014. Staging of hepatocellular carcinoma. *Journal of clinical*
822 *and experimental hepatology* 4, S74–S79.
- 823 El-Serag, H.B., Marrero, J.A., Rudolph, L., Reddy, K.R., 2008. Diagnosis
824 and treatment of hepatocellular carcinoma. *Gastroenterology* 134, 1752–
825 1763.

- 826 Ge, R., Yang, G., Chen, Y., Luo, L., Feng, C., Ma, H., Ren, J., Li, S., 2019a.
827 K-net: Integrate left ventricle segmentation and direct quantification of
828 paired echo sequence. *IEEE transactions on medical imaging* 39, 1690–
829 1702.
- 830 Ge, R., Yang, G., Chen, Y., Luo, L., Feng, C., Zhang, H., Li, S., 2019b. Pv-
831 lvnet: Direct left ventricle multitype indices estimation from 2d echocar-
832 diograms of paired apical views with deep neural networks. *Medical image*
833 *analysis* 58, 101554.
- 834 Ghesu, F.C., Georgescu, B., Mansi, T., Neumann, D., Hornegger, J., Co-
835 maniciu, D., 2016. An artificial agent for anatomical landmark detection
836 in medical images, in: *International conference on medical image comput-*
837 *ing and computer-assisted intervention*, Springer. pp. 229–237.
- 838 Ghesu, F.C., Georgescu, B., Zheng, Y., Grbic, S., Maier, A., Hornegger, J.,
839 Comaniciu, D., 2017. Multi-scale deep reinforcement learning for real-time
840 3d-landmark detection in ct scans. *IEEE transactions on pattern analysis*
841 *and machine intelligence* 41, 176–189.
- 842 Hamaguchi, R., Fujita, A., Nemoto, K., Imaizumi, T., Hikosaka, S., 2018.
843 Effective use of dilated convolutions for segmenting small object instances
844 in remote sensing imagery, in: *2018 IEEE winter conference on applications*
845 *of computer vision (WACV)*, IEEE. pp. 1442–1450.
- 846 von Herbay, A., Vogt, C., Haussinger, D., 2002. Late-phase pulse-inversion
847 sonography using the contrast agent levovist: differentiation between
848 benign and malignant focal lesions of the liver. *American Journal of*
849 *Roentgenology* 179, 1273–1279.
- 850 Huppertz, A., Balzer, T., Blakeborough, A., Breuer, J., Giovagnoni, A.,
851 Heinz-Peer, G., Laniado, M., Manfredi, R.M., Mathieu, D.G., Mueller,
852 D., et al., 2004. Improved detection of focal liver lesions at mr imaging:
853 multicenter comparison of gadoxetic acid-enhanced mr images with intra-
854 operative findings. *Radiology* 230, 266–275.
- 855 Isola, P., Zhu, J.Y., Zhou, T., Efros, A.A., 2017. Image-to-image transla-
856 tion with conditional adversarial networks, in: *Proceedings of the IEEE*
857 *conference on computer vision and pattern recognition*, pp. 1125–1134.